

# Dynamics of Tropical Low-Frequency Waves: An Analysis of the Moist Kelvin Wave\*

BIN WANG

*Department of Meteorology, University of Hawaii, Honolulu, Hawaii*

(Manuscript received 19 August 1987, in final form 1 March 1988)

## ABSTRACT

Stability of the equatorial atmosphere to a quasi-zonal, low frequency (order of  $10^{-6} \text{ s}^{-1}$ ) disturbance is investigated, using a model that consists of a two-layer free atmosphere and well-mixed boundary layer. The inclusion of boundary layer convergence leads to a circulation-dependent heating more nearly in accord with the behavior of numerically simulated low-frequency waves.

Slowly eastward moving unstable waves were found in a parameter regime stable to inviscid wave-CISK. The instability depends crucially upon the vertical distribution of the moist static energy of the basic state. A derived instability criterion suggests that amplification occurs when the condensational heating supported jointly by interior wave convergence and frictional convergence dominates over the dissipations due to longwave radiation and boundary layer viscosity.

The unstable waves exhibit preferred planetary scales. Since the vertical distribution of moist static energy of the basic state is closely related to sea surface temperature (SST), with increasing SST the growth rate increases for all wavelength, but the preferred scales shifts to shorter wavelength. The boundary layer convergence plays an important role in spatial scale selection. It not only suppresses unbounded growth of short waves, but also couples barotropic and baroclinic components in such a way that the generation of wave available potential energy is most efficient for planetary scales.

In the presence of boundary layer friction, the amplitude of an unstable wave in the zonal wind (or geopotential) at the upper level is significantly larger than that at the lower level. The phases between the two levels differ by about  $180^\circ$ . The slow eastward movement results mainly from the interior wave-induced reduction of static stability and thermal damping.

Behaviors of model unstable waves appear to resemble the observed 40–50 day mode in many aspects, such as vertical structure, energy source, zonal phase propagations, characteristic zonal and meridional scales, and its relation to SST. Limitations of the model are also discussed.

## 1. Introduction

The spectral peak corresponding to 41–53 day period was first detected by Madden and Julian (1971), using zonal wind and surface pressure data at Canton Island ( $3^\circ\text{S}$ ,  $172^\circ\text{W}$ ). They suggested that the oscillation is the result of eastward movement of circulation cell oriented in the equatorial zonal plane (Madden and Julian 1972). In recent years, some general characteristics of the phenomenon have been extensively documented in terms of outgoing longwave radiation (OLR) (e.g., Weickmann 1983; Lau and Chan 1985; Murakami et al. 1986) and divergent circulation (e.g., Lorenc 1984; Krishnamurti et al. 1985). It has been further noticed that the variations in monsoon activity and midlatitude circulation tend to associate and interact with the trop-

ical variations in this time scale (e.g., Krishnamurti and Subrahmanyam 1982; Liebmann and Hartmann 1984; Weickmann et al. 1985; Lau and Phillips 1986; Murakami 1988). Its relation to El Niño–Southern Oscillation (ENSO) is also noteworthy (Lau and Chan 1985). It seems that the nature of this low frequency wave needs to be understood if the cause of westerly anomalies in this time scale over the Pacific Ocean and their roles in triggering ENSO event are to be revealed.

Many essential features of the phenomenon have been recently simulated using various versions of a general circulation model (GCM) (Lau and Lau 1986; Hayashi and Sumi 1986; Hayashi and Golder 1986). The numerical model counterparts for an atmospheric 40–50 day oscillation are indeed caused by planetary scale, wavelike, eastward propagating circulation modes which are mainly confined within  $15^\circ$  latitude from the equator and vertically penetrate the entire troposphere with a baroclinic structure. The simulated phase speed tends to be greater than observed; however, a model with higher resolution may yield a comparable phase speed (Hayashi and Golder 1986). In what follows, this 40–50 day circulation mode will be referred to as a low frequency wave. The term “low frequency”

\* Contribution No. 87-13 of the Department of Meteorology, University of Hawaii.

Corresponding author address: Dr. Bin Wang, Dept. of Meteorology, University of Hawaii, 2525 Correa Road, Honolulu, Hawaii 96822.

here means a frequency  $O(10^{-6} \text{ s}^{-1})$ , corresponding to a characteristic period of 45 days.

The observational discoveries and numerical experiments have led to several attempts to develop an analytical theory on the low frequency oscillations. Response of the equatorial atmosphere to a localized heat source pulsating with a 40–50 day period was examined by Yamagata and Hayashi (1984) in an attempt to reveal the role of stationary forcing in exciting low frequency motion. Since OLR analysis suggests an thermal forcing that is migratory rather than stationary, consideration of a heat source interactive with large scale flow is more relevant.

Chang (1977) studied Kelvin wave-CISK (Conditional Instability of the Second Kind) in the presence of cumulus friction and Newtonian cooling and advanced the first significant interpretation for the horizontal and vertical structures of the low frequency oscillation. Using a five-level model, Lau and Peng (1987) and Chang and Lim (1987) showed that the slow eastward propagation may result from interactions between two vertical modes due to wave-CISK heating. Emanuel (1987) considered unstable waves driven by sea surface flux of moist entropy. Neelin et al. (1987) described this mechanism as evaporation–wind feedback. The eastward propagation of the unstable mode depends on the coefficient of surface heat exchange, the air–sea equivalent potential temperature difference, and the difference of the absolute temperature across the depth of the lower troposphere. Though this evaporation–wind feedback mechanism was shown to be important to the amplitude of the spectral peak corresponding to the 30–60 day oscillation in an idealized GCM model, the existence of the oscillation does not depend on it (Neelin et al. 1987).

While a firm observational basis has been established for various aspects of the low frequency oscillation, many fundamental questions have not been well understood. For instance, what factor controls the phase speed and causes slow eastward propagation? In addition to the above controversial interpretations of wave-CISK and evaporation–wind feedback, Chao (1987) argued that the coupled Kelvin–Rossby wave driven by a steady, traveling heat source should move with a weighted mean speed somewhere between speeds of Kelvin and Rossby waves. Yet, his results show that phase speed is dependent on the strength of dissipation and the size of the convective region.

Another issue is why the low frequency waves have a characteristic planetary zonal scale. Linear instabilities resulting from the Kelvin wave-CISK and evaporation–wind feedback all favor small scales. The use of conditional CISK heating (i.e., heat is released only in ascending region) was reported to suppress the unbounded short-wave growth (Lau and Peng 1987). Yet, several previous CISK studies using conditional heating did not find such an effect (e.g., Syono and Yamasaki

1966; Koss 1975). Other conjectures in regard to possible causes for wave selection also need to be elucidated or verified, including the effect of convection-suppressing downdrafts occurring in a finite longitudinal domain (Hayashi and Sumi 1986), and the effects of finite amplitude (Emanuel 1987) and dissipation (Chao 1987).

Previous theoretical studies of tropical low-frequency waves have not properly taken into account the boundary layer frictionally induced moisture convergence, so that the perturbation heating is controlled either by wave convergence or by zonal wind anomaly. As will be discussed in section 2, GCM experiment suggests that we cannot rule out boundary layer convergence in specifying the location and strength of the heating for low frequency waves. Based on this consideration, section 3 presents a theoretical model that couples a two-layer free atmosphere with a barotropic boundary layer. We consider this model as the simplest model which contains basic ingredients for adequately describing dynamics of low frequency waves. In sections 4 through 7, we examine the stability of the equatorial atmosphere to low frequency, quasi-zonal disturbances and illuminate the dynamic roles of the boundary layer process. In the last section we discuss the relevance of model results to the tropical 40–50 day oscillation and some limitations of the model.

## 2. Some general considerations on the low-frequency waves

### a. The energy source

How are observed circulation anomalies propagating around the globe on a time scale of 30–60 days maintained against dissipation? This important question relates to the energetics on this time scale. On the basis of observations, we assume that the low frequency wave has the following characteristic scales:

frequency	$\Sigma = 10^{-6} \text{ s}^{-1}$
zonal length	$L_x = 10^7 \text{ m}$
meridional length	$L_y = 10^6 \text{ m}$
vertical length	$L_z = 10^4 \text{ m}$
zonal velocity	$U_x = 5 \text{ m s}^{-1}$
meridional velocity	$U_y = U_x L_y / L_x$

Assume for the equatorial  $\beta$ -parameter,  $\beta = 2\Omega/a = 2 \times 10^{-11} \text{ m}^{-1} \text{ s}^{-1}$ , and for the static stability parameter,  $S_0 = (T/\theta)\partial\theta/\partial z = 3^\circ \text{C km}^{-1}$  in the equatorial region.

The characteristic scales of geopotential, temperature and vertical velocity can be deduced from the horizontal momentum equation, the hydrostatic equation and the thermodynamic equation successively. The results show that, if there were no diabatic heating, the vertical velocity scale would be

$$W_{ad} = \frac{\sum H}{S_0 R L_z} \max(\sum U_x L_x, U_y^2, \beta L_y^2 U_x) \\ = O(10^{-2} \text{ cm s}^{-1}),$$

where  $R$  denotes the gas constant,  $H$  the density scale height, and  $\max(\ )$  means the maximum of the quantity within parentheses. The corresponding horizontal divergence, from the continuity equation, should be  $O(10^{-8} \text{ s}^{-1})$ . Since vorticity is  $O(5 \times 10^{-6} \text{ s}^{-1})$ , such a weak divergence cannot make any significant contribution to the vorticity balance on a 30–60 day time scale, thus the motion must be barotropic. To maintain the observed baroclinic structure of the oscillation mode (e.g., the zonal wind and geopotential at 150 and 850 mb are nearly out of phase), the divergence-induced vorticity change must be of the same order as that of the temporal change of the vorticity. That requires an  $O(5 \times 10^{-7} \text{ s}^{-1})$  divergence field, which must be sustained by diabatic heating.

On the other hand, one may question whether the rate of precipitation heating associated with the low frequency wave is sufficiently large to force an  $O(5 \times 10^{-7} \text{ s}^{-1})$  divergence motion. At the present time, it is difficult to estimate accurately this heating rate due to the lack of observed rainfall data over the ocean. However, there is evidence that, over the global tropical region, the standard deviation of the 30–60 day components of the OLR is about one-third of that of the total OLR (Wang and Murakami 1987). It is plausible, for the purpose of estimating the order of magnitude, to conjecture that the standard deviation of daily precipitation due to 30–60 components is also about one-third of that of the total daily precipitation. If we further assume that the standard deviation of the daily precipitation has the same order of magnitude as the mean daily precipitation which is an order of  $10 \text{ mm day}^{-1}$ , then the precipitation rate associated with the low frequency wave should be  $O(3 \text{ mm day}^{-1})$ . This precipitation rate will produce an  $O(0.6 \text{ cm s}^{-1})$  vertical velocity and a divergence field of  $O(6 \times 10^{-7})$  which is large enough to affect the vorticity balance and maintain its baroclinic structure.

The foregoing scale analysis agrees with the results of previous observational and numerical studies. The low frequency wave was shown to be thermally direct in the sense of a net conversion of eddy available potential to eddy kinetic energy over this frequency range (Krishnamurti et al. 1985). A GFDL GCM simulation estimates that the precipitation rate associated with 30–60 day wave is  $O(2 \text{ mm day}^{-1})$  (Lau et al. 1988), which is close to the scaling argument here. It is concluded that the precipitational heating is a principal energy source for low frequency oscillations. Therefore, the mathematical representation of the diabatic heating is a crucial element of the model for low frequency motion.

### b. Condensational heating and boundary layer frictional effects

A detailed vertical structure of the 30–60 day oscillation mode simulated by a simplified GCM has been recently diagnosed (Lau et al. 1988). Results reveal that regions of precipitational heating are closely associated with upward motion and moisture convergence and exhibit a westward phase tilt with height in the lower troposphere, especially in the boundary layer. It is noted that the maximum heating in the middle troposphere has a spatial phase lag with low level moisture convergence at the top of the boundary layer. Therefore, an adequate representation is needed to take into account the spatial phase relationship between the heating and circulation.

To further analyze what might cause this notable westward phase tilt of the convergence and upward motion, we compare flow field at 850 mb with that of surface level (990 mb) obtained by the numerical simulation (Lau et al. 1988). At 830 mb the wind-geopotential relation resembles that of inviscid Kelvin waves near the equator. The zonal wind dominates and geostrophic balance between pressure and wind fields is pronounced. However, near sea level, the surface wind is less zonal and the frictionally induced cross-isobaric component causes significant convergence (divergence) in equatorial low (high) pressure anomalies. This suggests that the atmospheric heating is not only controlled by inviscid equatorial wave motion, but also linked to the boundary layer friction-induced convergence. This effect was noticed by Hayashi (1971) in his wave-CISK study.

Besides the potential role in specifying the location and strength of the precipitational heating, the boundary layer friction is also an efficient energy sink for the low frequency motion. Although veering angles over oceanic boundary layer are generally significantly smaller than those over midlatitude land, the net loss of kinetic energy is at least as large as that in the midlatitude because small pressure gradients lead to especially large ratio of kinetic energy dissipation to generation (Gray 1972). In the next section, we shall formulate a model consisting of both free atmosphere and boundary layer.

## 3. The model

### a. Interior "free" atmosphere

Observed low frequency motion possesses anisotropic horizontal length and velocity scales, i.e.,  $L_x \gg L_y$  and  $U_x \gg U_y$ . Near the equator, where the low frequency motion exhibits its maximum amplitude, the meridional component seems to be vanishingly small, especially at the upper troposphere. To simplify our analysis, we shall assume that the meridional compo-

nent of motion can be neglected above the planetary boundary layer.

To capture gross baroclinic structure of the low frequency motion, the simplest approximation for free atmosphere is a two-level model as depicted in Fig. 1; where  $p_s$ ,  $p_e$  and  $p_u$  stand for pressures at the surface, the top of boundary layer and the upper boundary (say, tropopause), respectively. The free atmosphere has been divided by pressure  $p_1$ ,  $p_2$  and  $p_3$  with equal pressure depth.

We consider small amplitude motion about a rest state on equatorial  $\beta$ -plane. Writing horizontal momentum and continuity equations at levels  $p_1$  and  $p_3$  and thermodynamic equation at  $p_2$ , and expressing vertical derivatives by centered difference of resolution  $\Delta p$  (half-depth of the free atmosphere), we obtain

$$\frac{\partial u_1}{\partial t} = -\frac{\partial \phi_1}{\partial x}, \quad (3.1a)$$

$$\beta y u_1 = -\frac{\partial \phi_1}{\partial y}, \quad (3.1b)$$

$$\frac{\partial u_1}{\partial x} + \frac{\omega_2 - \omega_u}{\Delta p} = 0, \quad (3.1c)$$

$$\frac{\partial u_3}{\partial t} = -\frac{\partial \phi_3}{\partial x}, \quad (3.1d)$$

$$\beta y u_3 = -\frac{\partial \phi_3}{\partial y}, \quad (3.1e)$$

$$\frac{\partial u_3}{\partial x} + \frac{\omega_e - \omega_2}{\Delta p} = 0, \quad (3.1f)$$

$$\frac{\partial}{\partial t} (\phi_3 - \phi_1) + S_2 \Delta p \omega_2 = \frac{R \Delta p}{C_p p_2} Q_2. \quad (3.1g)$$

In the above equations,  $C_p$  is specific heat at constant pressure;  $\omega_u$ ,  $\omega_2$  and  $\omega_e$  are vertical  $p$ -velocity at  $p_u$ ,  $p_2$  and  $p_e$ , respectively;  $Q_2$  denotes perturbation heating

rate per unit mass at  $p_2$ ; and  $S_2$  represents the static stability parameter:

$$S_2 = -\frac{1}{\theta_2 \rho_2} \frac{\theta_3 - \theta_1}{\Delta p}, \quad (3.2)$$

where  $\rho_2$  is the density of the basic state at  $p_2$  and  $\theta_1$ ,  $\theta_2$ ,  $\theta_3$  are potential temperatures of the basic state at  $p_1$ ,  $p_2$ ,  $p_3$ , respectively.

Introducing barotropic and baroclinic components of zonal winds and geopotentials defined by

$$\bar{u} = \frac{1}{2} (u_3 + u_1), \quad \bar{\phi} = \frac{1}{2} (\phi_3 + \phi_1), \quad (3.3a)$$

$$\tilde{u} = \frac{1}{2} (u_3 - u_1), \quad \tilde{\phi} = \frac{1}{2} (\phi_3 - \phi_1), \quad (3.3b)$$

The sums and differences of corresponding momentum and continuity equations at level  $p_1$  and  $p_3$  then yield

$$\frac{\partial \bar{u}}{\partial t} = -\frac{\partial \bar{\phi}}{\partial x}, \quad (3.4a)$$

$$\beta y \bar{u} = -\frac{\partial \bar{\phi}}{\partial y}, \quad (3.4b)$$

$$\frac{\partial \bar{u}}{\partial x} + \frac{1}{2 \Delta p} (\omega_e - \omega_u) = 0, \quad (3.4c)$$

$$\frac{\partial \tilde{u}}{\partial t} = -\frac{\partial \tilde{\phi}}{\partial x}, \quad (3.4d)$$

$$\beta y \tilde{u} = -\frac{\partial \tilde{\phi}}{\partial y}, \quad (3.4e)$$

$$\frac{\partial \tilde{u}}{\partial x} + \frac{1}{2 \Delta p} (\omega_e + \omega_u - 2\omega_2) = 0. \quad (3.4f)$$

If the upper boundary condition:

$$\omega_u = 0 \quad \text{at} \quad p = p_u \quad (3.5)$$

is used, the continuity equations (3.4c) and (3.4f) become, respectively

$$\omega_e = -2 \Delta p \frac{\partial \bar{u}}{\partial x}, \quad (3.6)$$

$$\omega_2 = \frac{1}{2} \omega_e + \Delta p \frac{\partial \tilde{u}}{\partial x}. \quad (3.7)$$

The thermodynamic equation (3.1g) is then expressed as

$$\frac{\partial \tilde{\phi}}{\partial t} + C_0^2 \frac{\partial \tilde{u}}{\partial x} = -\frac{C_0^2}{2 \Delta p} \omega_e - \frac{R \Delta p}{2 C_p p_2} Q_2 \quad (3.8)$$

where

$$C_0 = \left( \frac{S_2 \Delta p^2}{2} \right)^{1/2} \quad (3.9)$$

is the long gravity wave speed of the gravest baroclinic mode.

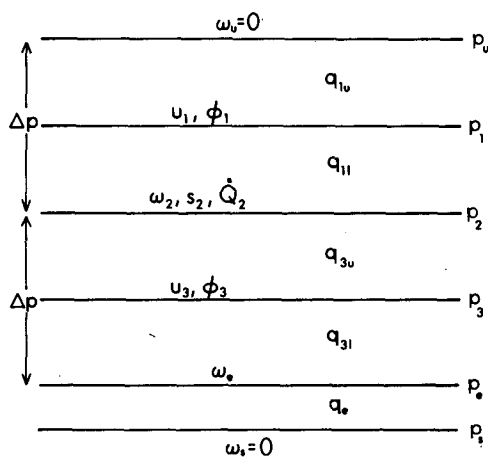


FIG. 1. Schematic vertical structure of the model.

### b. Representation of diabatic heating for low frequency motions

Only two major heating processes will be included in the present model—condensational latent heat and longwave radiation. The condensational heating in the tropics is chiefly released by cumulus ensembles associated with various weather systems. Conceptually, there exists direct interaction between cumulus convection and mesoscale system (e.g., cloud cluster). However, mesoscale disturbances should preferably occur in a region of moisture convergence provided by planetary scale, low frequency waves. Since the low-level convergence associated with low frequency waves is weaker than that of cloud cluster scale, one might assume that cumulus ensembles are directly organized by mesoscale systems, which are in turn modulated by the low-frequency wave convergence. On the other hand, although convective latent heat is mainly consumed by the development of cloud clusters or other mesoscale disturbances, the net residual heat that is transported and spread out by these disturbances is presumably sufficient to enhance and sustain the low frequency planetary waves. This secondary cooperative interaction between planetary and cloud cluster scale motions differs from the direct interaction between cumulus and cloud cluster motions. Yet, our assumption here is that the amount of precipitation corresponding to the residual heating is proportional to the moisture convergence induced by the low frequency waves. Therefore, the condensational heating rate associated with the low frequency motion may be parameterized on the basis of moisture and heat budget, following Kuo (1974) and Stevens and Lindzen (1978).

Assuming that a fraction  $(1 - b)$  of the total moisture convergence goes into changing the atmospheric vapor mixing ratio, we may write the net precipitation rate  $P$  as the sum of the moisture convergence into an atmospheric column of unit cross section and the local surface evaporation rate,  $E$ . In terms of present model parameters,

$$P = b \left[ - \int_{p_u}^{p_s} \nabla \cdot (\bar{q}(p) \mathbf{v}) \frac{dp}{g} + E \right] \\ = - \frac{b}{g} [\omega_2(\bar{q}_3 - \bar{q}_1) + \omega_e(\bar{q}_e - \bar{q}_3)] + bE, \quad (3.10)$$

where  $\bar{q}_e$ ,  $\bar{q}_3$  and  $\bar{q}_1$  represent mean vapor mixing ratio in the layers  $(p_s, p_e)$ ,  $(p_e, p_2)$  and  $(p_2, p_u)$  respectively, where  $(p_i, p_j)$  denotes the layer between  $p_i$  and  $p_j$ . Both the moisture convergence and surface evaporation here are presumably induced by the low frequency perturbation only. Since the surface evaporation rate associated with the low frequency motion is about an order of magnitude smaller than the precipitation rate, especially between  $10^\circ\text{S}$  and  $10^\circ\text{N}$  (Lau et al. 1988), for simplicity, in the following analysis we shall neglect the effect of evaporation anomaly.

Assuming that latent heat is released to change the thickness  $2\bar{\phi} = \phi_3 - \phi_1$  of the layer between  $p_1$  and  $p_3$ , the condensational heating rate at  $p_2$  is simply  $PL_Cg/\Delta p$ , where  $L_C$  is the latent heat and  $g$  the gravity. We assume that longwave radiation in the free atmosphere takes a Newtonian cooling form. Thus, the total diabatic heating rate at  $p_2$  for the low frequency disturbance can be written as

$$Q_2 = - \frac{bL_C}{\Delta p} [\omega_2(\bar{q}_3 - \bar{q}_1) \\ + \omega_e(\bar{q}_e - \bar{q}_3)] + \mu \frac{2C_p p_2}{R\Delta p} \bar{\phi}, \quad (3.11)$$

where  $\mu$  is a constant coefficient for Newtonian cooling.

### c. Boundary layer

A boundary layer is needed to evaluate the vertical  $p$ -velocity at the bottom of the free atmosphere,  $\omega_e$ . It should be noted that even if the meridional component,  $v$ , is vanishingly small above the boundary layer, it may be generated by frictional and earth's rotational effects within the boundary layer. Since it makes a significant contribution to convergence, it must be included in the boundary layer model.

Perturbation equations for a steady, barotropic, neutral boundary layer flow have the form:

$$-\beta y v = - \frac{\partial \phi_3}{\partial x} + g \frac{\partial \tau_{xp}}{\partial p}, \quad (3.12a)$$

$$\beta y u = - \frac{\partial \phi_3}{\partial y} + g \frac{\partial \tau_{yp}}{\partial p}, \quad (3.12b)$$

$$\frac{\partial \omega}{\partial p} = - \left( \frac{\partial u}{\partial x} + \frac{\partial v}{\partial y} \right), \quad (3.12c)$$

where we have assumed that the pressure is continuous across the interface between the boundary layer and free atmosphere at  $p = p_e$ . Additional matching conditions require that the vertical velocity and turbulent Reynolds stresses ( $\tau_{xp}$ ,  $\tau_{yp}$ ) are continuous at  $p_e$ , namely:

$$\omega \text{ be continuous, and } (\tau_{xp}, \tau_{yp}) = 0 \text{ at } p = p_e. \quad (3.13a)$$

At the lower boundary,  $p = p_s$ , a slip condition suitable for turbulent flow (Eliassen 1971) is used. The Reynolds stress is related to the surface wind by a simple linearized stress relationship, i.e.,

$$(\tau_{xp}, \tau_{yp}) = -\rho_e K_D (u_s, v_s) \text{ at } p = p_s, \quad (3.13b)$$

where  $K_D$  is a measure of the surface drag and  $u_s = u(p_s)$ ,  $v_s = v(p_s)$ . To determine  $K_D$ , we subdivide the boundary layer into a surface layer and an outer boundary layer (Blackadar and Tennekes 1968). In the outer boundary layer, (3.13a, b, c) applies while

in the surface layer the Reynolds stress is nearly constant, and the wind profile is logarithmic. Matching the outer boundary layer with the surface layer at their interface leads to

$$K_D = A_z \left/ \left[ h \ln \left( \frac{h}{z_0} \right) \right] \right., \quad (3.14)$$

where  $A_z$  is turbulent viscosity,  $h$  the depth of the surface layer and  $z_0$  the surface roughness length.

Integrating (3.13a, b, c) with respect to  $p$  from  $p_e$  to  $p_s$ , dividing the resulting equations by  $(p_s - p_e)$ , and using conditions (3.13a, b) and (3.3a, b), we obtain

$$-\beta y v_B = -\frac{\partial}{\partial x} (\bar{\phi} + \tilde{\phi}) - \frac{\rho_e g}{p_s - p_e} K_D u_B, \quad (3.15a)$$

$$\beta y u_B = -\frac{\partial}{\partial y} (\bar{\phi} + \tilde{\phi}) - \frac{\rho_e g}{p_s - p_e} K_D v_B, \quad (3.15b)$$

$$\omega_e = (p_s - p_e) \left( \frac{\partial u_B}{\partial x} + \frac{\partial v_B}{\partial y} \right), \quad (3.15c)$$

where

$$u_B = \frac{1}{p_s - p_e} \int_{p_e}^{p_s} u dp, \quad (3.16a)$$

$$v_B = \frac{1}{p_s - p_e} \int_{p_e}^{p_s} v dp \quad (3.16b)$$

are vertically averaged horizontal winds in the boundary layer. In derivation of (3.15), we have assumed that the surface winds  $u_s$  and  $v_s$ , are equal to  $u_B$  and  $v_B$ , respectively. In (3.15a, b), the frictional force for vertically averaged boundary layer flow takes a simple "Reyleigh form" at the price of complete neglect of the changes in wind direction within the boundary layer. Gray's (1972) mean statistics indicated that changes in wind direction through the lowest kilometer are small (about  $10^\circ$ ) over the tropical oceans. The model simplification seems not to be severely restricted.

#### 4. The basic results

##### a. Nondimensional equations

It is convenient to write the equations in a nondimensional form, using the length scale  $(C_0/\beta)^{1/2}$ , the time scale  $(\beta C_0)^{-1/2}$ , the horizontal velocity scale  $C_0$ , the geopotential scale  $C_0^2$ , and the vertical  $p$ -velocity scale  $2\Delta p(\beta C_0)^{1/2}$ . The nondimensional equations for model free atmosphere can then be obtained from (3.4a, b, d, e), (3.6) and (3.8) with the aid of (3.11). The resulting equations are

$$\frac{\partial \bar{u}}{\partial t} = -\frac{\partial \bar{\phi}}{\partial x}, \quad (4.1a)$$

$$y \bar{u} = -\frac{\partial \bar{\phi}}{\partial y}, \quad (4.1b)$$

$$\frac{\partial \bar{u}}{\partial x} + \omega_e = 0, \quad (4.1c)$$

$$\frac{\partial \bar{u}}{\partial t} = -\frac{\partial \bar{\phi}}{\partial x}, \quad (4.1d)$$

$$y \bar{u} = -\frac{\partial \bar{\phi}}{\partial y}, \quad (4.1e)$$

$$\left( \frac{\partial}{\partial t} + N \right) \bar{\phi} + (1 - I) \frac{\partial \bar{u}}{\partial x} = (B - 1) \omega_e, \quad (4.1f)$$

where the nondimensional numbers are

$$N = \mu / \sqrt{\beta C_0}, \quad (4.2)$$

$$I = (\bar{q}_3 - \bar{q}_1) / \alpha, \quad (4.3)$$

$$B = (2\bar{q}_e - \bar{q}_3 - \bar{q}_1) / \alpha, \quad (4.4)$$

$$\alpha = 2C_p p_2 C_0^2 / (R b L_c \Delta p). \quad (4.5)$$

Nondimensional number  $N$  measures the intensity of the Newtonian cooling;  $I$  and  $B$  are coefficients of heating contributed by the interior wave convergence and boundary layer convergence, respectively. Since  $C_0^2 = S_2 \Delta p^2 / 2$ , the quantity,  $\alpha$ , may be regarded as a nondimensional measure of static stability of the basic state. Both  $I$  and  $B$  depend on  $\alpha$ .

The nondimensional forms of the boundary layer equations (3.15a, b, c) are

$$-y v_B = -\frac{\partial}{\partial x} (\bar{\phi} + \tilde{\phi}) - E_k u_B, \quad (4.6a)$$

$$y u_B = -\frac{\partial}{\partial y} (\bar{\phi} + \tilde{\phi}) - E_k v_B, \quad (4.6b)$$

$$\omega_e = \frac{p_s - p_e}{2\Delta p} \left( \frac{\partial u_B}{\partial x} + \frac{\partial v_B}{\partial y} \right), \quad (4.6c)$$

where

$$E_k = \frac{\rho_e g A_z}{(p_s - p_e) \sqrt{\beta C_0} h \ln(h/z_0)}. \quad (4.7)$$

We now seek solutions to (4.1a-f) and (4.6a-c) of the form:

$$(\bar{u}, \bar{u}, \bar{\phi}, \tilde{\phi}, u_B, v_B, \omega_e) = R_e [\bar{U}(y), \tilde{U}(y), \bar{\Phi}(y), \tilde{\Phi}(y), U_B(y), V_B(y), \Omega_e(y)] e^{i(kx - \sigma t)}, \quad (4.8)$$

where  $k$  and  $\sigma$  are dimensionless zonal wavenumber and frequency, respectively. Substituting (4.8) into (4.1a, b, d, e) and integrating with respect to  $y$  yield

$$\bar{U} = \frac{k}{\sigma} \bar{\Phi}, \quad (4.9)$$

$$\tilde{U} = \frac{k}{\sigma} \tilde{\Phi}, \quad (4.10)$$

$$\bar{\Phi} = \bar{\Phi}(0) e^{-(ky^2)/(2\sigma)}, \quad (4.11)$$

$$\tilde{\Phi} = \tilde{\Phi}(0)e^{-(ky^2)/(2\sigma)}. \quad (4.12)$$

We observe that only when frequency  $\sigma$  possesses a positive real part ( $\sigma_r > 0$ ), the wave has an equatorial trapped structure; namely, the wave amplitude vanishes as  $|y| \rightarrow \infty$ , in accordance with equatorial  $\beta$ -plane approximation (Matsuno 1966). Solutions corresponding to  $\sigma_r < 0$  implies unbounded increase of amplitude as  $|y| \rightarrow \infty$  and must be excluded.

*b. Vertical velocity at the top of the boundary layer*

Substitution of (4.8), (4.11) and (4.12) into (4.6a, b, c) gives

$$u_B = (\tilde{\Phi} + \tilde{\Phi}) \frac{-ikE_k + \frac{k}{\sigma} y^2}{E_k^2 + y^2}, \quad (4.13)$$

$$v_B = (\tilde{\Phi} + \tilde{\Phi}) \frac{\frac{k}{\sigma} E_k y + iky}{E_k^2 + y^2}, \quad (4.14)$$

$$\Omega_e = \frac{k(p_s - p_e)(\tilde{\Phi} + \tilde{\Phi})}{2\Delta p(E_k^2 + y^2)\sigma} \left[ E_k \left( 1 + k\sigma - \frac{k}{\sigma} y^2 \right) + i\sigma - \frac{2y^2(E_k + i\sigma)}{E_k^2 + y^2} \right]. \quad (4.15)$$

Equations (4.13) through (4.15) indicate that the boundary layer flow can be determined by the geopotential field above the boundary layer when the interior motion is zonal.

The friction-induced vertical velocity,  $\omega_e$ , is symmetric about the equator and bounded everywhere. It

is important to observe that the strongest friction-induced vertical motion occurs at the equator. Away from the equator,  $\omega_e$  decreases exponentially with increasing latitude.

Taking characteristic values for equatorial tropospheric parameters listed in Table 1, we find  $C_0 = 49 \text{ m s}^{-1}$ ,  $\sqrt{C_0/\beta} = 1460 \text{ km}$ ,  $\sqrt{\beta C_0} = 2.9 \text{ day}^{-1}$ . For motions with 40–50 day period, the nondimensional frequency:

$$|\sigma| \ll 1. \quad (4.16a)$$

In the equatorial region between  $5^\circ\text{S}$  and  $5^\circ\text{N}$ ,

$$y^2 \leq 0.1 \ll 1. \quad (4.16b)$$

For motions with wavelength longer than 10 000 km, nondimensional wavenumber

$$k < 1. \quad (4.16c)$$

Using Eq. (4.7) and the model parameters listed in Table 1, we find that the Ekman number:

$$E_k = 1.07 = O(1). \quad (4.16d)$$

On the basis of the above estimations for nondimensional variables and parameters, if (4.16a, b, c, d) are used in (4.15), to the lowest order,  $O(1)$ , we attain

$$\Omega_e = \frac{kD}{\sigma} (\tilde{\Phi} + \tilde{\Phi}), \quad (4.17)$$

where

$$D = \frac{p_s - p_e}{2\Delta p E_k}, \quad (4.18)$$

which measures the strength of the boundary layer dis-

TABLE 1. Basic model parameters and nondimensional numbers. The equations of definition are indicated by the numbers in the brackets.

$\beta$	Equatorial $\beta$ -parameter ( $\beta = 2\Omega/a$ )		$2.3 \times 10^{-11} \text{ m}^{-1} \text{ s}^{-1}$
$\Delta p$	Pressure depth of the half free atmosphere		40 kPa
$p_2$	Pressure at the middle of the free atmosphere		50 kPa
$p_s - p_e$	Pressure depth of the boundary layer		10 kPa
$\theta_1$	Potential temperature at 300 mb		340.1 K
$\theta_2$	Potential temperature at 500 mb		325.6 K
$\theta_3$	Potential temperature at 700 mb		312.7 K
$\mu$	Newtonian cooling coefficient		$1.5 \times 10^{-5} \text{ s}^{-1}$
$A_z$	Boundary layer turbulent viscosity		$10 \text{ m}^2 \text{ s}^{-1}$
$z_0$	Surface roughness length		0.01 m
$h$	Depth of the surface layer		40 m
$b$	Fractional moisture converted into rainfall		0.9
$H$	Density scale height		7.6 km
$H_1$	Water vapor scale height		2.2 km
$q_s$	Surface mixing ratio		0.019
$\bar{q}_1$	Mean mixing ratio between 500 and 100 mb		0.0004
$S_2$	Static stability parameter at $p_2$	(3.2)	$3 \times 10^{-6} \text{ m}^2 \text{ s}^{-2} \text{ Pa}^{-2}$
$C_0$	Long gravity wave speed of the gravest baroclinic mode	(3.9)	$49 \text{ m s}^{-1}$
$\alpha$	Nondimensional measure of the $S_2$	(4.5)	$9.33 \times 10^{-3}$
$N$	Strength of the Newtonian cooling	(4.2)	0.447
$D$	Strength of the boundary layer dissipation	(4.18)	0.116
$I$	Intensity of interior wave convergence	(4.3)	0.847
$B$	Intensity of friction-induced convergence	(4.4)	2.67

sipation. We shall use (4.17) to approximate the vertical velocity at the lower boundary of the free atmosphere,  $p = p_e$ .

### c. Dispersion relation

Substituting (4.8) into (4.1c) gives

$$\bar{U} = \frac{i}{k} \Omega_e. \quad (4.19)$$

Using (4.9) and (4.17), we find

$$\bar{\Phi} = \frac{iD}{k - iD} \bar{\Phi}. \quad (4.20)$$

The dispersion relation can be obtained by the use of (4.8), (4.10), (4.17) and (4.20) in the thermodynamic equation (4.1f):

$$\sigma = -i \frac{N}{2} + \left[ -\frac{N^2}{4} + k^2(1 - I) + \frac{ikD}{1 - iD/k} (B - 1) \right]^{1/2}. \quad (4.21)$$

We note that only the positive sign in front of the complex square root in (4.21) was taken, which corresponds to an eastward moving trapped wave. The growth rate and zonal phase speed can then be derived from (4.21):

$$kC_i = -\frac{N}{2} \pm \frac{1}{\sqrt{2}} (\sqrt{A_r^2 + A_i^2} - A_r)^{1/2}, \quad (4.22)$$

$$C_r = \frac{1}{\sqrt{2}k} (\sqrt{A_r^2 + A_i^2} + A_r)^{1/2}, \quad (4.23)$$

where

$$A_r = k^2(1 - I) - \frac{N^2}{4} - \frac{D^2}{1 + D^2/k^2} (B - 1), \quad (4.24a)$$

$$A_i = \frac{kD}{1 + D^2/k^2} (B - 1). \quad (4.24b)$$

In (4.22), the positive (negative) sign in front of the second rhs term is taken when  $B > 1$  ( $B < 1$ ).

In the absence of diabatic heating and boundary layer friction, (4.21) reduces to  $\sigma = k$ , recovering equatorially trapped Kelvin waves. If the condensational heating is caused solely by Kelvin wave induced convergence, as hypothesized in inviscid Kelvin wave-CISK, (4.21) gives

$$\sigma = k\sqrt{1 - I},$$

implying that amplifying inviscid wave-CISK mode occurs as  $I > 1$ , and the corresponding phase speed vanishes but the growth rate increases unbounded with decreasing wavelength: the instability favors smallest cumulus scale. In the case of multilevel model, eastward moving modes could be found, but the unbounded

growth remains for the shortest wave (e.g., Chang and Lim 1987). The condition:

$$I < 1 \quad (4.25)$$

corresponds to a *stable* parameter regime for inviscid wave-CISK. Using (4.3), this condition can be rewritten as

$$\bar{q}_3 - \bar{q}_1 < \alpha. \quad (4.26)$$

For typical equatorial atmospheric parameters listed in Table 1, this condition is generally satisfied. In what follows we shall focus our attention on this stable regime of wave-CISK.

## 5. The growth rate and zonal phase speed

### a. Instability criterion

Before performing numerical calculations, it is useful to have general information about the marginal instability.

Equation (4.22) shows that for the stable regime of inviscid wave-CISK, i.e.,  $I < 1$ , the addition of the boundary-layer moisture convergence creates instability and the amplification of the unstable wave requires

$$\gamma > \gamma_c, \quad (5.1)$$

where

$$\gamma = D(B - 1), \quad (5.1a)$$

$$\gamma_c = N(1 + D^2/k^2) \left[ \left( 1 - I + \frac{N^2 D^2}{4k^4} \right)^{1/2} - \frac{ND}{2k^2} \right]. \quad (5.1b)$$

Quantity  $\gamma$  represents the net contribution to instability of the boundary layer friction. In the presence of moisture, the boundary layer friction plays dual roles. On one hand, it dissipates kinetic energy as implied by the term  $-D$  in (5.1a). On the other, it contributes to the generation of eddy potential energy through supplying the moisture convergence needed for condensational heating in the warm region. This positive contribution is described by the term  $BD$  in (5.1a). The higher the boundary layer moisture content  $\bar{q}_e$  (or the greater the value of  $B$ ), the more efficient this positive effect to the development. Thus, the frictional effect may enhance wave growth when  $B > 1$ , or, using (4.4), when

$$2\bar{q}_e - (\bar{q}_3 + \bar{q}_1) > \alpha. \quad (5.2)$$

Criterion (5.1), therefore, states that the low frequency instability occurs when the net destabilizing effect of the boundary-layer moisture convergence, designated by  $\gamma$ , exceeds a critical value  $\gamma_c$ . For fixed wavenumber, the critical value  $\gamma_c$  decreases as the wave-induced moisture convergence ( $I$ ) increases and/or the thermal damping ( $N$ ) decreases. In this sense, the low frequency instability found in the stable regime of in-



viscid wave-CISK arises from the condensational heating jointly supported by free atmospheric wave motion and friction-induced boundary layer convergence. Instability takes place when their combined effects dominate over those of longwave radiational cooling and boundary layer dissipation.

It is important to notice that, for fixed thermal and mechanical dissipations, the instability threshold,  $\gamma_c$ , is a monotonic function of wavenumber  $k$ , moreover:

$$\lim_{k \rightarrow \infty} \gamma_c = N\sqrt{1 - I}, \quad (5.3a)$$

$$\lim_{k \rightarrow 0} \gamma_c = D(1 - I). \quad (5.3b)$$

Under typical conditions (e.g., the parameters listed in Table 1),  $N > D\sqrt{1 - I}$ , thus

$$D(1 - I) < \gamma_c < N\sqrt{1 - I}, \quad (5.4)$$

implying that the preferred marginally unstable wave occurs at longwave limit. In other words, when  $\gamma = D(B - 1)$  increases from zero, the longest wave will become unstable first. This is one of the noticeable features different from inviscid wave-CISK.

#### b. Dependence of instability on wavelength and vertical distribution of moisture

Equations (4.22) and (4.23) indicate that both the growth rate and zonal phase speed are functions of wavelength. They also depend on nondimensional numbers,  $I$ ,  $B$ ,  $\alpha$ ,  $N$  and  $D$ , namely, the vertical distribution of moisture content ( $\bar{q}_e$ ,  $\bar{q}_3$ ,  $\bar{q}_1$ ), the static stability of the basic state ( $S_2$ ), and the strengths of Newtonian cooling ( $N$ ) and boundary layer dissipation ( $D$ ).

The model parameters along with estimated nondimensional numbers are given in Table 1. The potential temperatures are annual means in the tropical belt between 7.5°S and 7.5°N computed from Oort and Rasmusson's (1971) statistics. The turbulent viscosity,  $A_z$ , depth of surface layer,  $h$ , and surface roughness length,  $z_0$ , are taken typical values for planetary boundary layer. The Newtonian cooling coefficient  $\mu$  is taken from Holton and Colton (1972). The mean mixing ratios,  $\bar{q}_e$  and  $\bar{q}_3$  are computed using the following empirical formula:

$$\begin{aligned} \bar{q}(p_1, p_2) &= \frac{1}{p_2 - p_1} \int_{p_1}^{p_2} q(p) dp \\ &= q_s \frac{(p_2^m - p_1^m)}{m(p_2 - p_1)}, \end{aligned} \quad (5.5)$$

where  $p$ ,  $p_1$  and  $p_2$  are nondimensional pressures;  $\bar{q}(p_1, p_2)$  denotes mean mixing ratio of the layer between  $p_1$  and  $p_2$ ;  $q_s$  represents the vapor mixing ratio at the surface  $p = p_s$ ; and  $m$  is defined by

$$m = \frac{H}{H_1}, \quad (5.6)$$

where  $H$  and  $H_1$  are density and water vapor scale height, respectively. The derivation of (5.5) is presented in the Appendix. The value for  $q_s$  in Table 1 is not global zonal mean, but representative over warm ocean when SST is between 28 and 28.5°C. The value  $m = 3.5$  corresponds to density scale height  $H = 7.6$  km and water vapor scale height  $H_1 = 2.2$  km as suggested by Tomasi (1984) for equatorial Indian Ocean.

Figure 2 shows growth rate and zonal phase speed as functions of wavelength for typical atmospheric parameters listed in Table 1. A notable feature is the existence of a maximum growth rate of about 0.1 day<sup>-1</sup> at wavelength around 24 000 km. This preferred wave has an eastward phase speed about 17 m s<sup>-1</sup> relative to the basic state, approximately 1/3 of the long gravity wave speed  $C_0$ .

Table 2 shows crucial dependence of the instability on the vertical distribution of moisture content. The growth rate increases with both increasing  $\bar{q}_e$  and  $\bar{q}_3$ . However, as shown in Table 3, the effects of  $\bar{q}_e$  and  $\bar{q}_3$  on zonal phase speed are different. The increase in  $\bar{q}_3$  enhances latent heat release and reduces static stability of the basic state, thus slowing down eastward propagation. On the other hand, an increase in  $\bar{q}_e$  speeds up eastward movement because heating due to the boundary-layer moisture convergence tends to lead the maximum upward motion and the interior moisture convergence.

#### 6. Structures of unstable waves

Characteristic meridional structures of unstable waves are given by (4.9) through (4.12). Using (4.8) and (4.12), we can write

$$\begin{aligned} \tilde{\phi} &= R_e \left\{ \tilde{\Phi}(0) \exp \left[ \sigma_i t - \frac{k\sigma_r}{2|\sigma|^2} y^2 \right. \right. \\ &\quad \left. \left. + i \left( kx + \frac{k\sigma_i}{2|\sigma|^2} y^2 - \sigma_r t \right) \right] \right\}. \end{aligned} \quad (6.1)$$

For eastward propagating unstable wave, the amplitude attains its maximum at the equator and decays exponentially away from the equator with an  $e$ -folding scale:

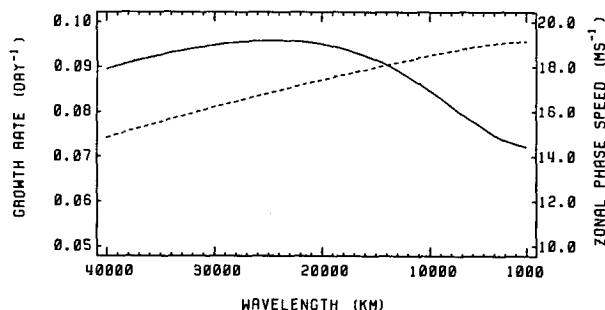


FIG. 2. The growth rate (solid) and zonal phase speed (dashed) as functions of wavelength for low frequency unstable waves. Parameters used in computation are listed in Table 1.

TABLE 2. Dependence of the growth rate ( $\text{day}^{-1}$ ) on the mean mixing ratio in the boundary layer,  $\bar{q}_e$ , and in the lower free atmosphere,  $\bar{q}_3$ , for wavelength 20 000 km. Other parameters are the same as listed in Table 1.

$\bar{q}_3 \times 10^3$	$\bar{q}_e \times 10^3$			
	14.0	15.0	16.0	17.0
6.5	-0.16	-0.10	-0.05	-0.01
7.5	-0.09	-0.04	0.01	0.05
8.5	0.00	0.04	0.08	0.12
9.5	0.09	0.13	0.16	0.19

$$l_y = \left[ \frac{2(C_r + C_i^2/C_r)}{\beta} \right]^{1/2}. \quad (6.2)$$

Since  $l_y < (2C_0/\beta)^{1/2}$ , which is the equatorial Rossby radius of deformation, the unstable waves are more tightly trapped near the equator compared to free equatorial Kelvin waves. Equation (6.1) also reveals a meridional tilt of constant phase lines (Chang 1977). Any amplifying (decaying) wave is bound to have a poleward (equatorward) phase propagation.

The vertical structure of unstable waves is dominantly baroclinic. From (4.20), we may rewrite

$$\tilde{\Phi} = \sqrt{1 + k^2/D^2} e^{i(\pi+\theta_1)} \bar{\Phi}, \quad (6.3)$$

where

$$\theta_1 = \arctan(k/D). \quad (6.4)$$

Therefore, the amplitude ratio of the baroclinic to barotropic modes,  $(1 + k^2/D^2)^{1/2}$ , depends on wavelength and the strength of the boundary layer dissipation. It is evident that for short waves the barotropic component is negligibly small compared to the baroclinic one. For planetary wave one or two and  $D = 0.12$  as used in Table 1, (6.3) yields an amplitude ratio approximately between 2 and 4. Thus, the baroclinic mode is still dominant. In a vertically continuous model with a rigid lid, there is a continuous spectrum of modes. Since the diabatic heating in the tropics tends to be a maximum at midtroposphere, we expect that the gravest baroclinic mode remains a major component of the motion.

We now consider phase relationships among geopotential ( $\bar{\phi}$  and  $\tilde{\phi}$ ), zonal wind ( $\bar{u}$  and  $\tilde{u}$ ) and vertical  $p$ -velocity  $\omega_e$ . Equation (6.3) discloses that  $\bar{\phi}$  and  $\tilde{\phi}$  are nearly, but not exactly, out of phase. Zonal wind  $\bar{u}$  ( $\tilde{u}$ ) lags behind geopotential  $\bar{\phi}$  ( $\tilde{\phi}$ ) by an acute phase angle:

$$\theta_2 = \arctan(C_i/C_r), \quad (6.5)$$

as implied by (4.9) and (4.10). Equation (4.19) indicates that the barotropic zonal wind  $\bar{u}$  leads vertical  $p$ -velocity at the top of boundary layer,  $\omega_e$ , exactly by a quarter of cycle. Using (4.17) and (4.20), we find

$$\Omega_e = \frac{k^2 D}{|\sigma|(k^2 + D^2)^{1/2}} e^{i\theta_3} \tilde{\Phi}, \quad (6.6)$$

where

$$\theta_3 = \arctan\left(\frac{D\sigma_r - k\sigma_i}{k\sigma_r + D\sigma_i}\right) \quad (6.7)$$

so that friction-induced upward motion leads the negative thickness  $\tilde{\phi}$  (or positive temperature anomaly) by a phase angle  $\theta_3$  which is wavenumber-dependent.

In a summary, the model unstable waves exhibit the following zonal phase relationships:

$$\tilde{\phi} \xrightarrow[\pi+\theta_1]{\theta_2\bar{u}} \bar{\phi} \xrightarrow[\pi/2]{\omega_e} \tilde{u} \xrightarrow[\pi/2]{\omega_e} \tilde{\phi}. \quad (6.8)$$

In (6.8), the arrows specify the direction of decrease in zonal phase; the angles beneath the arrows are corresponding spatial phase differences between two adjacent fields. Angles  $\theta_1$ ,  $\theta_2$  and  $\theta_3$  are defined by (6.4), (6.5) and (6.7), respectively. It is easy to show that the sum of  $\theta_1$ ,  $\theta_2$  and  $\theta_3$  is  $\pi/2$ .

## 7. The mechanism for scale selection

Contrasting to the short-wave "blow-up" of the inviscid wave-CISK, the growth rate of unstable waves in the present model is bounded for short waves. From (4.22), it can be shown that

$$\lim_{k \rightarrow \infty} kC_i = \frac{1}{2} \left[ \frac{D(B-1)}{(1-I)^{1/2}} - N \right], \quad (7.1)$$

and the corresponding phase speed is only a fraction of the long gravity wave speed due to the interior heating:

$$\lim_{k \rightarrow \infty} C_r = \sqrt{1-I}. \quad (7.2)$$

In the case of inviscid wave-CISK, the heating is spatially in phase with the wave-induced low level convergence, thus a direct feedback causes convective instability. In the present model, heating associated with boundary-layer moisture convergence leads interior wave convergence by a spatial phase difference less than a quarter of wavelength. Because of this spatial phase shift, the moisture supply in the boundary layer is not controlled by the heat-driven secondary circulation itself so that direct convective instability is suppressed.

TABLE 3. As in Table 2 but for the phase speed in units of  $\text{m s}^{-1}$ .

$\bar{q}_3 \times 10^3$	$\bar{q}_e \times 10^3$			
	14.0	15.0	16.0	17.0
6.5	20.0	21.1	22.2	23.2
7.5	16.0	17.5	18.8	20.0
8.5	12.6	14.3	15.8	17.2
9.5	9.8	11.6	13.2	14.7

This mechanism is similar to what was discussed by Wang (1987). The suppression of unbounded short-wave growth by temporal phase lag between low-level moisture convergence and release of condensational heat was discussed by Davies (1979).

It is more interesting to note that the presence of boundary layer friction couples baroclinic and barotropic components. This dynamic coupling favors instabilities in planetary scales. To demonstrate this, it is illustrative to consider a model in which heating forces only the baroclinic mode. Replace the rigid lid at  $p = p_u$  by a free surface and assume

$$\omega_u = \omega_e, \quad \text{at } p = p_u. \quad (7.3)$$

It follows from (3.4c) that  $\partial \tilde{u} / \partial x = 0$ , implying the absence of the perturbation barotropic component. Although (7.3) is, to a large extent, artificial, it allows us to examine an idealized case in which the baroclinic component decouples with barotropic component. In such a system, the wave motion is governed by:

$$\frac{\partial \tilde{u}}{\partial t} = -\frac{\partial \tilde{\phi}}{\partial x}, \quad (7.4a)$$

$$\beta y \tilde{u} = -\frac{\partial \tilde{\phi}}{\partial y}, \quad (7.4b)$$

$$\omega_2 = \omega_e + \Delta p \frac{\partial \tilde{u}}{\partial x}, \quad (7.4c)$$

$$\frac{\partial \tilde{\phi}}{\partial t} + \frac{S_2 \Delta p}{2} \omega_2 = -\frac{R \Delta p}{2 C_p p_2} Q_2, \quad (7.4d)$$

where  $Q_2$  is given by (3.11). The equations for boundary layer are the same as (3.15a, b, c) except  $\tilde{\phi} = 0$ . By an analysis parallel to that in section 4, we find complex frequency:

$$\sigma = -i \frac{N}{2} + \left[ k^2(1 - I) - \frac{N^2}{4} + ikD(B' - 2) \right]^{1/2}, \quad (7.5)$$

where

$$B' = 2(\bar{q}_e - \bar{q}_1)/\alpha; \quad (7.6)$$

other symbols have been defined before.

We now compare the frequency given by (7.5) with that given by (4.21). For short waves, (4.21) becomes, approximately

$$\sigma = -i \frac{N}{2} + \left[ k^2(1 - I) - \frac{N^2}{4} + ikD(B - 1) \right]^{1/2}, \quad (7.7)$$

Since, in general,  $B - 1 > B' - 2$ , the growth rate calculated by (7.5) is smaller than that by (7.7). This suggests that neglect of barotropic component results in reduction of the growth rate for short waves.

More importantly, the qualitative difference between (7.5) and (4.21) becomes significant for planetary scale

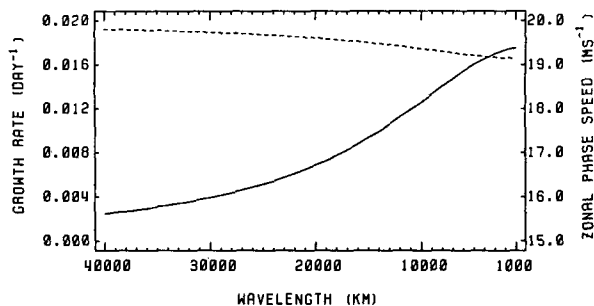


FIG. 3. Growth rate (solid) and phase speed (dashed) calculated using (7.5) for the model containing baroclinic mode only. Notice that the graphic scales for the growth rate and zonal phase speed are different from Fig. 2.  $q_e = 0.192$  is used, other parameters are as in Table 1.

waves. Analysis of (7.5) reveals that the growth rate of baroclinic mode monotonically increases with decreasing wavelength and no wave selection exists. Figure 3 confirms this qualitative inference. Comparing solution (7.5) with (4.21) leads to a conclusion that the dynamic coupling and interaction between the baroclinic and barotropic components are responsible for the selection of the preferred planetary scales.

The explanation is as follows. In the presence of boundary layer friction, heating associated with frictional convergence depends on the sum of the baroclinic and barotropic components,  $\tilde{\phi} + \bar{\phi}$  [Eq. (4.17)]. The barotropic component  $\bar{\phi}$  is sustained by compression (stretching) of the air column due to frictional convergence/divergence in a model with rigid lid, whereas the baroclinic component is affected by adiabatic cooling (heating) due to friction-induced vertical motion and by the diabatic heating, a part of which is also linked to boundary layer moisture convergence. The two vertical modes are not spatially in phase. Accordingly, the friction-induced upward motion and heating lead positive temperature anomaly by a phase angle  $\theta_3$  which is wavenumber-dependent as shown by (6.7). The rate of generation of eddy available potential energy is proportional to the correlation between the perturbation heating and temperature, or  $\omega_e$  and  $\tilde{\phi}$ ; it may achieve maximum at certain planetary scales, depending on the moisture content and the strength of dissipation. Thus, the planetary scale is preferred. Without the coupling between  $\bar{\phi}$  and  $\tilde{\phi}$ ,  $\omega_e$  is in phase with  $\tilde{\phi}$  and the rate of generation of eddy energy is simply proportional to wavenumber, so that the shortest wave grows fastest.

## 8. Discussions

Observations suggest that the 40–50 day oscillation in the tropics is caused by eastward movement of planetary scale waves that consist of circulation and convection anomalies (e.g., Madden and Julian 1972; Lorenc 1984; Weickmann et al. 1985). Numerical simulations appear to support this notion and further

provide information on detailed structures of composite waves (e.g., Lau and Lau 1986). In this section we intend to explain, in terms of model results, some of the characteristics concerning low frequency waves.

### a. Baroclinic structures

Madden and Julian (1971) found that 1) the oscillation in zonal wind at 150 and 850 mb are nearly out of phase, 2) zonal wind anomalies in lower troposphere are in phase with surface pressure anomalies, and 3) negative temperature anomalies are associated with positive surface pressure anomalies. Figure 4a shows longitudinal variations of zonal winds and geopotentials subtracted from the composite structure of 30–60 day waves simulated by a simplified GCM (Lau et al. 1988). The upper levels are taken 100 mb for geopotential and 200 mb for zonal wind, in accordance with the levels their maximum amplitudes occur. To facilitate comparison, we also present in Fig. 4b the baro-

tropic and baroclinic components of geopotential and zonal wind along with vertical  $p$ -velocity at 900 mb. The baroclinic geopotential component is proportional to negative thickness (or positive temperature) between 850 and 100 mb. The surface pressure anomaly is almost exactly in phase with 850 mb geopotential and thus not given. It is seen from Fig. 4a and 4b that structure of the simulated wave agrees well with the three features observed by Madden and Julian.

We note from Fig. 4b that 1) the amplitudes of baroclinic components are three to four times as large as those of barotropic components, 2)  $\tilde{\phi}$  and  $\bar{\phi}$  are nearly out of phase, 3) geopotentials  $\tilde{\phi}$  and  $\bar{\phi}$  lead zonal wind  $\tilde{u}$  and  $\bar{u}$  respectively by about  $\pi/5$ , 4)  $\tilde{u}$  leads  $\omega_e$  by about  $3\pi/5$ , and 5)  $\omega_e$  leads  $\bar{\phi}$  by about  $\pi/5$ . All of these features can be qualitatively explained by (6.3) and (6.8), which describe the vertical structures and phase-relationships for the model unstable low-frequency waves.

### b. The energy source for instability

The baroclinic structure of the unstable wave is a manifestation of direct heating-driven circulation. The scale analysis shows that precipitation heating associated with low frequency wave can generate a divergence field which is strong enough to affect the vorticity balance and maintain the baroclinic structure. The present model demonstrates that the instability crucially depends on the vertical distribution of moist static energy of the basic state (Tables 2 and 3). The interior wave-induced and boundary layer friction-induced convergence jointly supply moist energy to amplify or maintain unstable waves against the energy losses due to longwave radiation and boundary layer dissipation.

### c. Anisotropic horizontal length scales

The tropical low frequency waves are confined meridionally to low latitude (perhaps mainly between 20°S and 20°N) with maximum amplitude located along the equator. They also exhibit a zonal scale of planetary wave one or two. The equatorially trapped meridional structure of the model unstable wave results from the effect of the variation of the Coriolis parameter. The characteristic  $e$ -folding trapping scale given by (6.2) is less than the equatorial radius of deformation  $\sqrt{2C_0/\beta}$  which is about 2000 km. Within reasonable parameter range, the model unstable waves also exhibit preferred planetary scales.

The analysis in section 7 suggests that the boundary layer friction may be important in selecting the preferred zonal scale. First, the friction-induced moisture convergence is maximum near the equator and leads interior wave convergence by an acute phase angle. This spatial phase shift prevents direct convective instability and suppresses growth of the shortwaves. More importantly, the boundary layer convergence couples the baroclinic and barotropic components in such a

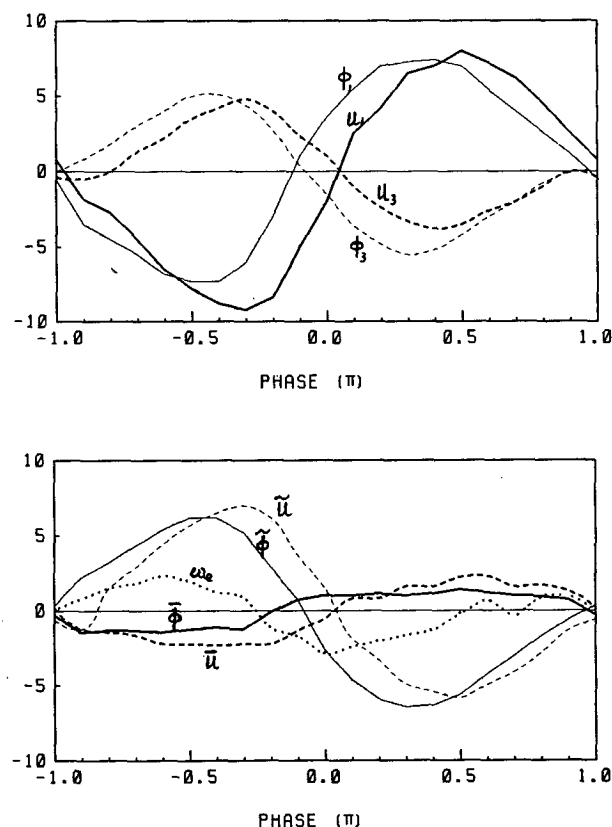


FIG. 4. Zonal variations of (a) geopotential at 100 mb ( $\phi_1$ ) and 850 mb ( $\phi_3$ ) and zonal wind at 200 mb ( $u_1$ ) and 850 mb ( $u_3$ ); (b) baroclinic and barotropic components of geopotential and zonal wind defined by (3.3), and vertical  $p$ -velocity at 900 mb ( $\omega_e$ ). The quantities  $\phi_1$ ,  $u_1$ ,  $\phi_3$ ,  $u_3$ , and  $\omega_e$  are subtracted from the composite structure of intraseasonal oscillation modes simulated by a simplified GCM (Lau et al. 1988). The values at  $-\pi$  and  $\pi$  have been taken their average to form an exact cycle. The units are  $\text{m s}^{-1}$  for zonal wind,  $10 \text{ m}^2 \text{ s}^{-2}$  for geopotential and  $5 \times 10^{-3} \text{ p s}^{-1}$  for  $\omega_e$ .

way that the generation of available potential energy due to the correlation of  $\omega$  and  $\bar{\phi}$  (or the perturbation heating and warming) may be favored for planetary scales.

#### d. The slow eastward propagation

The 40–50 day quasi-periodicity corresponds to a zonal phase speed of  $10 \text{ m s}^{-1}$  for wave one and  $5 \text{ m s}^{-1}$  for wave two. Phase speeds of model unstable waves, even after subtracting the speed of basic current ( $3\text{--}5 \text{ m s}^{-1}$ ), are still higher than these values for the given model parameters. Nevertheless, the model qualitatively shows that the latent heat release associated with interior wave convergence can substantially slow down the eastward propagation by reducing static stability (Table 3). Besides, a relatively strong thermal damping also favors slow eastward movement. These mechanisms were previously emphasized, one or another, by Lau and Peng (1987) and Chang (1977).

#### e. The relation to sea surface temperature (SST)

Intensity of the low frequency wave varies with longitude. The largest amplitude occurs over the Indian and western Pacific Oceans and it decreases somewhat as the waves transverse the eastern Pacific and Atlantic Oceans (e.g., Madden and Julian 1972; Krishnamurti et al. 1985; Murakami et al. 1986). The oscillation in OLR tends to be confined to the equatorial region of the Indian and western Pacific Oceans in non-El Niño years and to expand eastward into the central and eastern Pacific during ENSO events, suggesting a link between SST and strength of the oscillation (Lau and Chan 1985). Lau and Peng's (1987) numerical experiment confirms this finding.

The relationship between SST and low frequency instability can be understood if we express atmospheric moisture parameters as functions of SST. In the time scale of intraseasonal variation, the surface mixing ratio  $q_s$  is well correlated with SST and may be approximated by

$$q_s = (0.940 \times \text{SST} - 7.64) \times 10^{-3}, \quad (8.1)$$

where SST is in units of degrees Celsius. Equation (8.1) is derived based on monthly mean data subtracted from Hastenrath and Lamb (1979a,b). The correlation coefficient between  $q_s$  and SST is 0.977 and the error mean square is  $0.35 \times 10^{-3}$ . Using (8.1) and (5.5), one can estimate  $\bar{q}_e$  and  $\bar{q}_3$  directly from SST. The moisture content above 500 mb is assumed to be independent of SST.

Numerical calculations show that the growth rate increases with increasing SST for all wavelengths; for given model parameters, no growing wave is possible when SST is below  $25^\circ\text{C}$ . This suggests that a warm ocean surface, in general, favors development of low frequency waves. When the SST is higher than  $25^\circ$  but lower than  $27^\circ$ , wave one is most unstable with a rel-

atively small growth rate (less than  $0.05 \text{ day}^{-1}$ ). With further increasing SST, the most unstable wavelength decreases, while the maximum growth rate increases as shown in Fig. 5. When the SST exceeds  $29^\circ\text{C}$ , the short waves are favored, but their growth rate remains bounded. The dependence of wave selection on SST may be suggestive of the complexity of the phenomenon. In a coupled air-sea system, Lau and Shen (1988) found similar results and the air-sea interaction may also play a role in the wave selection.

#### f. The meridional phase propagation

A poleward phase propagation in zonal wind, divergence and OLR at a speed of about  $1 \text{ m s}^{-1}$  is observed to be associated with the eastward propagation, but seems to be confined to the Asian summer monsoon region (e.g., Krishnamurti and Subrahmanyam 1982; Krishnamurti et al. 1985; Murakami et al. 1986). Chang (1977) interpreted this poleward propagation or the meridional tilt of the wave axis as resulting from the instability itself.

Equation (6.1) shows that 1) the amplifying (decaying) waves move poleward (equatorward) and eastward, 2) the meridional phase speed decreases with latitude away from the equator, and 3) the ratio of meridional to zonal phase speed is  $2|\sigma|^2/\sigma_i$ . The first prediction appears to agree with observations over the Indian and western Pacific Oceans, but so far there are no observations of equatorward propagation in the eastern Pacific where the waves decay. The gradually slowing of the northward movement with latitude has not been reported yet. Since the ratio,  $2|\sigma|^2/\sigma_i$ , can be one-quarter to one-fifth, only when  $\sigma_i^2 \gg \sigma_r^2$  and  $\sigma_i = O(10^{-1})$ , implying that relatively large growth rate ( $\sim 0.3 \text{ day}^{-1}$ ) and slow zonal phase speed ( $\sim 5 \text{ m s}^{-1}$ ) are needed to match an observed northward phase speed of  $1 \text{ m s}^{-1}$ .

We note that Hayashi and Sumi's (1986) aqua-planet model failed whereas the model with land-ocean contrast and topography (Lau and Lau 1986; Hayashi and

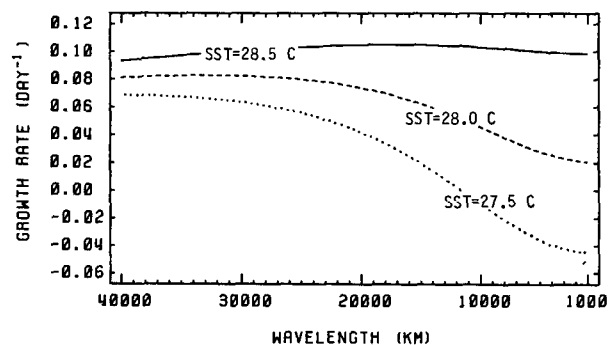


FIG. 5. The growth rate of unstable low frequency waves as function of wavelength for different sea surface temperature (SST). All parameters used in computation are the same as listed in Table 1 except the moisture parameter  $q_s$  which is calculated using (8.1).

Golder 1986) were able to simulate the northward propagation in the Asian summer monsoon region. This suggests that physical processes associated with land-sea thermal contrast, topography, and longitudinal variation of the SST could be important for the meridional phase propagation. This conjecture appears to be in conformity with the ground hydrological cycle mechanism suggested by Webster (1983) and the mechanism due to the advective effect of the Hadley circulation (Gaswami and Shukla 1984; Anderson and Stevens 1987). Further studies are needed in this regard.

It is realized that a full comprehension of the dynamics of the tropical low frequency motion requires a more complex dynamic framework. The present study using a prototype model is only the first step of the research, which focuses on the behavior of the moist Kelvin wave in the presence of boundary layer friction. In order to produce a model as simple as possible, we have made a number of assumptions. A linear circulation-dependent heating was employed, and it is not clear how the solution will differ if a more realistic conditional heating is used. The model also neglected evaporational heating associated with the waves, which may play certain roles in low frequency instability as shown in numerical experiment (Neelin et al. 1987).

In view of the sensitivity of the solution to vertical distribution of the moisture content, it is worthwhile to explore the behavior of the instability in a continuous model. The influence of a more realistic vertical and zonal distribution of circulation-dependent heating on the low frequency instability needs also to be clarified in terms of a continuous model.

Some numerical experiments suggest that,  $10^{\circ}$ – $15^{\circ}$  latitude away from the equator, the horizontal structure of the low frequency wave bears resemblance to Rossby wave in which the  $v$ -component is significant (Hayashi and Golder 1986; Hayashi and Sumi 1986). Chao (1987) emphasized the role of Rossby wave in the interpretation of the meridional structure of low frequency waves. To make the problem analytically tractable, we have neglected the meridional component of the free atmospheric motion and assumed that the friction-induced vertical motion has the same structure as that of geopotential in lower free atmosphere. The consequences of these crucial simplifications should be addressed in terms of a model including the  $v$ -component. It is also interesting to determine the roles of the coupling between Kelvin and long Rossby waves through frictional moisture convergence and associated heating in the dynamics of the tropical low frequency waves. These issues are currently being investigated.

**Acknowledgments.** The author wishes to thank Dr. N.-C. Lau who kindly provided results of numerical experiments which motivated this research. I would also thank Dr. K. M. Lau for his careful review and invaluable suggestions. This leads to my consideration

of the coupling between the barotropic and baroclinic components. Thanks are extended to Drs. T. Murakami and C. Name for their helpful discussions and reading the manuscript, to Mrs. S. Arita typing the manuscript, and to Mr. X.-L. Wang and Ms. H.-L. Rui for graphical assistance.

This research was supported by NOAA Grant NA85ABH00032.

## APPENDIX

### Derivation of the Empirical Formula (5.5)

The observed absolute humidity,  $\rho_w$ , decreases exponentially in the tropical atmosphere. It can be well estimated, below 5 km, by (e.g., Tomasi 1984):

$$\rho_w(z) = \rho_w(0)e^{-z/H_1}, \quad (\text{A1})$$

where  $z$  is the height measured from the surface and  $H_1$  is water-vapor scale height.

Consider an isothermal atmosphere for which the density is

$$\rho(z) = \rho(0)e^{-z/H}, \quad (\text{A2})$$

where  $H$  is density scale height. Specific humidity  $q'(z)$  can then be computed by

$$q'(z) = \frac{\rho_w}{\rho} = q'_s e^{-z(1/H_1 - 1/H)}, \quad (\text{A3})$$

where  $q'_s = \rho_w(0)/\rho(0)$  is surface specific humidity. Using  $z = H \ln(p/p_0)$  in (A3), we obtain:

$$q'(p) = q'_s \left( \frac{p}{p_s} \right)^{H/H_1 - 1}, \quad (\text{A4})$$

where  $p_s$  is the surface pressure. Defining  $p/p_s$  as non-dimensional pressure, and integrating (A4) from  $p_1$  to  $p_2 > p_1$ , we then obtain (5.5) if we neglect the small difference between the mixing ratio and the corresponding specific humidity.

## REFERENCES

- Anderson, J. R., and D. E. Stevens, 1987: The response of the tropical atmosphere to low frequency thermal forcing. *J. Atmos. Sci.*, **44**, 676–686.
- Blackadar, A. K., and H. Tenneker, 1968: Asymptotic similarity in neutral barotropic planetary boundary layer. *J. Atmos. Sci.*, **25**, 1015–1020.
- Chang, C.-P., 1977: Viscous internal gravity waves and low frequency oscillations in the tropics. *J. Atmos. Sci.*, **34**, 901–910.
- , and H. Lim, 1987: Kelvin wave-CISK: A possible mechanism for the 30–50 day oscillations. *J. Atmos. Sci.*, **44**, in press.
- Chao, W.-C., 1987: On the origin of the tropical intraseasonal oscillation. *J. Atmos. Sci.*, **44**, 1940–1949.
- Davies, H. C., 1979: Phase-lagged wave-CISK. *Quart. J. Roy. Meteor. Soc.*, **105**, 325–353.
- Eliassen, A., 1971: On the Ekman layer in a circular vortex. *J. Meteorol. Soc. Japan*, **49** (Special issue), 784–789.
- Emanuel, K. A., 1987: An air-sea interaction model of intraseasonal oscillations in the tropics. *J. Atmos. Sci.*, **44**, 2324–2340.
- Gaswami, B. N., and J. Shukla, 1984: Quasi-periodic oscillations in a symmetrical general circulation model. *J. Atmos. Sci.*, **41**, 20–37.

- Gray, W. M., 1972: A diagnostic study of the planetary boundary layer over the oceans. *Dynamics of the Tropical Atmosphere*, NCAR, 587 pp.
- Hastenrath, S., and P. J. Lamb, 1979a: Climatic atlas of the Indian Ocean. I. Surface climate and atmospheric circulation. The University of Wisconsin Press.
- , and —, 1979b: Climatic atlas of the tropical Atlantic and eastern Pacific Oceans. The University of Wisconsin Press.
- Hayashi, Y., 1971: Large-scale equatorial waves destabilized by convective heating in the presence of surface friction. *J. Meteorol. Soc. Japan*, **49**, 450–457.
- , and D. G. Golder, 1986: Tropical intraseasonal oscillations appearing in a GFDL general circulation model and FGGE data. Part I. Phase propagation. *J. Atmos. Sci.*, **43**, 3058–3067.
- , and A. Sumi, 1986: The 30–40 day oscillations simulated in an "Aqua Planet" model. *J. Meteorol. Soc. Japan*, **64**, 451–467.
- Holton, J. R., and D. E. Colton, 1972: A diagnostic study of the vorticity balance at 200 mb in the tropics during the northern summer. *J. Atmos. Sci.*, **29**, 1124–1128.
- Koss, W. J., 1975: Linear stability analysis of CISK-induced low latitude disturbances. NOAA Tech. Memo. EFL WMP0-24, 176 pp. (NTIS No. PB-248450).
- Krishnamurti, T. N., and D. Subrahmanyam, 1982: The 30–50 day mode at 850 mb during MONEX. *J. Atmos. Sci.*, **39**, 2088–2095.
- , P. K. Jayakumar, J. Sheng, N. Surgi and A. Kumar, 1985: Divergent circulations on the 30 to 50 day time scale. *J. Atmos. Sci.*, **42**, 364–375.
- Kuo, H.-L., 1974: Further studies of the parameterization of the influences of cumulus convection on large scale flow. *J. Atmos. Sci.*, **31**, 1232–1240.
- Lau, K. M., and P. H. Chan, 1985: Aspects of the 40–50 day oscillation during the northern winter as inferred from outgoing longwave radiation. *Mon. Wea. Rev.*, **113**, 1889–1909.
- , and T. J. Phillips, 1986: Coherent fluctuations of extratropical geopotential height and tropical convection in intraseasonal time scales. *J. Atmos. Sci.*, **43**, 1164–1181.
- , and L. Peng, 1987: Origin of low frequency (intraseasonal) oscillations in the tropical atmosphere. Part I: The basic theory. *J. Atmos. Sci.*, **44**, 950–972.
- , and S. Shen, 1988: On the dynamics of intraseasonal oscillation and ENSO. *J. Atmos. Sci.*, in press.
- Lau, N.-C., and K. M. Lau, 1986: The structure and propagation of intraseasonal oscillation appearing in a GFDL general circulation model. *J. Atmos. Sci.*, **43**, 2023–2047.
- , I. M. Held and J. D. Neelin, 1988: The Madden-Julian oscillation in an idealized GCM model. *J. Atmos. Sci.*, in press.
- Liebmann, B., and D. L. Hartmann, 1984: An observational study of tropical-midlatitude interaction on intraseasonal time scales during winter. *J. Atmos. Sci.*, **41**, 3333–3350.
- Lovenc, A. C., 1984: The evolution of planetary-scale 200mb divergent flow during the FGGE year. *Quart. J. Roy. Met. Soc.*, **110**, 427–441.
- Madden, R. A., and P. R. Julian, 1971: Detection of a 40–50 day oscillation in the zonal wind in the tropical Pacific. *J. Atmos. Sci.*, **28**, 702–708.
- , and —, 1972: Description of global-scale circulation cells in the tropics with a 40–50 day period. *J. Atmos. Sci.*, **29**, 1109–1123.
- Matsuno, T., 1966: Quasi-geostrophic motions in the equatorial area. *J. Meteorol. Soc. Japan*, **44**, 25–43.
- Murakami, T., 1988: Intraseasonal atmospheric teleconnection patterns during the Northern Hemisphere winter. *J. Climate*, **1**, No. 2.
- , L.-X. Chen, A. Xie and M. L. Shrestha, 1986: Eastward propagation of 30–60 day perturbations as revealed from outgoing longwave radiation data. *J. Atmos. Sci.*, **43**, 961–971.
- Neelin, J. D., I. M. Held and K. H. Cook, 1987: Evaporation–wind feedback and low frequency variability in the tropical atmosphere. *J. Atmos. Sci.*, **44**, 2341–2348.
- Oort, A. H., and E. M. Rasmusson, 1971: *Atmospheric Circulation Statistics*. U.S. Dept. of Commerce, 323 pp.
- Stevens, D. E., and R. S. Lindzen, 1978: Tropical wave-CISK with a moisture budget and cumulus friction. *J. Atmos. Sci.*, **35**, 940–961.
- Syono, S., and M. Yamasaki, 1966: Stability of symmetrical motions driven by latent heat release by cumulus convection under the existence of surface friction. *J. Meteorol. Soc. Japan*, Ser 2, **44**, 353–375.
- Tomasi, C., 1984: Vertical distribution features of atmospheric vapor in the Mediterranean, Red Sea, and Indian Ocean. *J. Geophys. Res.*, **89**, D2, 2563–2566.
- Wang, B., 1987: The nature of CISK in a generalized continuous model. *J. Atmos. Sci.*, **44**, 1411–1426.
- Wang, X.-L., and T. Murakami, 1987: Intraseasonal meridional surges and equatorial convections during the southern hemisphere summer. *J. Meteorol. Soc. Japan*, **65**, 727–736.
- Webster, P. J., 1983: Mechanisms of monsoon low-frequency variability: Surface hydrological effects. *J. Atmos. Sci.*, **40**, 4110–4124.
- Weickmann, K. M., 1983: Intraseasonal circulation and outgoing longwave radiation modes during Northern Hemisphere winter. *Mon. Wea. Rev.*, **111**, 1838–1858.
- , G. R. Lussy and J. E. Kutzbach, 1985: Intraseasonal (30–60 day) fluctuations of outgoing longwave radiation and 250 mb streamfunction during northern winter. *Mon. Wea. Rev.*, **112**, 941–961.
- Yamagata, T., and Y. Hayashi, 1984: A simple diagnostic model for the 30–50 day oscillation in the tropics. *J. Meteorol. Soc. Japan*, **62**, 709–717.